AMS Home Journals Home Journal Archive Subscribe For Authors Help Advanced Search Search Go

Full Text View

Hybrid Coastal and Interior Modes for Two-Dimensional Homogeneous Flow in a Cylindrical Ocean*

Onno Bokhove[+]

Woods Hole Oceanographic Institution, Woods Hole, Massachusetts

E. R. Johnson

University College London, London, England

ABSTRACT

Flows on coastal shelves and in the deep interior ocean are often considered separately, but transport of fluid between these two regions can have important biologial or environmental consequences. This paper considers a linear *coupled* coastal and deep interior-ocean model in the idealized context of a homogeneous two-dimensional cylindrical ocean with a rigid lid and axisymmetric step shelf topography. Both a semianalytical mode-matching approach and brute-force finite-element numerics have been used to analyze the linear dynamics. It is shown that hybrid planetary β-plane Rossby and topographic shelf modes emerge. The structure of these inviscid modes is clarified by considering their frequency dependence on shelf break radius, by contrasting the evolution of hybrid modes to the evolution of pure shelf and pure β-plane Rossby modes (considering streamfunction fields and particle paths), and by showing solutions of the initial value problem. Both "ocean" and "laboratory" parameter values are considered. Hybrid modes exchange information between the deep ocean and coastal shelves, especially at the intermediate frequencies where the separate planetary Rossby mode and topographic shelf mode dispersion curves overlap. The role of these modes is particularly clear in an initial value problem wherein a localized initial condition on the southern shelf later leads to large-scale interior ocean circulation. Forced–dissipative calculations reveal the sensitivity of resonantly generated hybrid Rossby–shelf modes to the strength of Ekman damping. For typical oceanic and laboratory parameter values hybrid modes are altered by increasing Ekman damping but do not disappear.

Options:
- Create Reference
- Email this Article
- Add to MyArchive
- Search AMS Glossary

Search CrossRef for:
- Articles Citing This Article

Search Google Scholar for:
- Onno Bokhove
- E. R. Johnson

1. Introduction

The problem of transport of fluid—with its salinity, potential vorticity, nutrient, and pollutant concentration—between shallow continental coastal shelves and deep ocean basins contains a variety of interesting but incompletely understood fluid dynamical aspects that are important for the understanding of biological processes and spread of coastal pollution into the open ocean. Our knowledge of the wind-driven variability over continental shelves is fairly sophisticated (e.g., Brink 1991), as is our knowledge of idealized basin-scale ocean circulation (e.g., Pedlosky 1996) but our knowledge of the combined ocean–shelf circulation, with a dynamical coupling between coastal shelf-wave dynamics and deep interior-ocean dynamics, is limited. In state-of-the-art ocean general circulation models (OGCMs) the numerical resolution is generally insufficient to

resolve coastal processes, and ocean boundaries in OGCMs are usually approximated by vertical walls at a certain depth contour close to the shelf break. A proper understanding of the nature of the interaction between coherent structures in the open oceans and coastal shelf-wave dynamics would be helpful in parametrizing coastal wave dynamics in OGCMs, and subsequently in an interpretation of simulation results. Observations indicate that the continental slope or shelf break often acts as a barrier to transport, although coherent eddies, for example, Gulf Stream rings (as seen in sea surface temperature satellite imagery), and wind-induced phase propagation (Kelly et al. 1993, 1998) do account for cross-shelf transport. Nevertheless a clear interpretation of observations of coupled coastal dynamics and deep interior ocean circulation appears to be missing. We apparently lack a theoretical framework of this coupling, even in the context of idealized homogeneous ocean circulation models, which could guide our observational and numerical investigations [more background is found in Huthnance (1987, 1995) for barotropic and stratified conditions, respectively]. Can we construct such a theoretical framework for linear and nonlinear interactions between coastal and deep interior ocean dynamics, first, in the context of homogeneous models and, second, in a stratified context with realistic topography?

To address this question the present investigation discusses the analysis of inviscid and forced–dissipative eigenmodes in a two-dimensional homogeneous ocean that contains topographically induced shelf waves and basin-scale planetary (β-plane) Rossby waves. A rigid-lid approximation is invoked and simplified step shelf topography is used; the former is in line with previous coastal wave studies (e.g., Power et al. 1989) and the latter is mathematically convenient and allows efficient mode matching. Stratification, nonlinearity, and nonhydrostatic (three-dimensional) effects are thus all omitted here despite their potential importance. These effects will be discussed briefly in the conclusions. In particular, for a step profile, superinertial two-dimensional topographic modes have three-dimensional trapped counterparts, while subinertial shelf modes appear to lead to radiation of three-dimensional vertical modes away from the topographic region of generation (Chapman 1982). The present linear analysis is a first study toward understanding the effects of cross-shelf flows on large-scale ocean circulation in a closed basin. In a normal mode analysis, hybrid modes are expected to exist in a frequency window where the separate shelf and Rossby wave dispersion curves overlap. Evaluation of this hybrid modal structure is the focus of our analysis.

Despite much work on identifying linear high-frequency gravitational modes in Laplace's tidal equations or, equivalently, in shallow water equations (e.g., Lamb 1993; Platzmann 1984) less attention has been paid to the nature of low-frequency hybrid topographic shelf and β-plane Rossby waves. Miller (1986) numerically studied the linear subinertial normal modes in a rectangular shallow water basin with rigid lid, β plane, and smooth shelf topography in an attempt to explain observed tide gauge records; he showed that a coupled oscillator solution in which the transport streamfunction is decomposed into a set of pure shelf mode and pure Rossby mode oscillators provides good convergence. He appears to have been the first to calculate basin-scale hybrid planetary Rossby and topographic shelf modes. Our calculations consist of two-dimensional numerical calculations and also a semianalytical mode-matching approach that reduces the eigenvalue problem to a one-dimensional numerical eigenvalue problem at the shelf break. This semianalytical approach provides a more detailed picture of emerging hybrid modes, allows more realistic shallow and narrow shelves, and is computationally more efficient, while the finite element approach extends more readily to the forced–dissipative regime. Dorr and Grimshaw (1986) used WKB techniques to investigate the hybrid nature of shelf and β-plane Rossby waves in the long-wave limit for a straight coast with shallow shelf topography decaying away exponentially fast to a constant deep interior-ocean depth at infinity. Their asymptotic results indicate again that hybrid Rossby–shelf modes are expected when separate dispersion curves overlap. In particular, our analysis complements and extends Dorr and Grimshaw's investigations by an explicit calculation of all—boundary trapped shelf, hybrid Rossby–shelf, and deep interior-ocean Rossby—normal modes and confirms their results for specific step shelf topography in an entire, closed ocean basin. Mode matching tracks the origin of the hybrid modes by showing frequency dependence as a function of relevant parameters, for example, shelf break radius or the height difference. This relation forms an alternative for the traditional dispersion diagrams that are no longer accessible because the linearized barotropic vorticity equation considered here has no separable solutions. Finally, we also present some forced–dissipative calculations and thus identify the resonant forced–dissipative counterparts of the free hybrid modes for reasonable general forcing profiles. All results are presented for a set of "oceanic" and "laboratory" parameter values, the latter with rotating tank experiments in mind.

Our plan of presentation is as follows: Section 2 introduces a rotating two-dimensional, homogeneous ocean model with abrupt shelf topography and β effect in a cylindrical ocean basin. Section 3 discusses the linear inviscid modes, considering their frequency dependence, particle paths, and the initial value problem. Section 4 gives the linear forced–dissipative modal response to harmonic forcing. Section 5 summarizes the results and discusses nonhydrostatic and nonlinear effects in homogeneous models, laboratory designs, and stratification.

2. Homogeneous model

The hydrostatic, shallow nature of the oceans and the influence of rotation suggest that the dynamics is governed by two-dimensional Taylor columns except in thin Ekman boundary layers. The two-dimensional horizontal momentum and continuity equations appear, familiar from studies in coastal oceanography,

$$\frac{\partial \mathbf{v}}{\partial t} + (\mathbf{v} \cdot \nabla)\mathbf{v} + f\mathbf{k} \times \mathbf{v}$$

$$= -\frac{1}{\rho_0}\nabla p + E_h \nabla^2 \mathbf{v} + \mathbf{F}(\mathbf{x}, t) - \alpha\frac{f\delta_E}{H_T(\mathbf{x})}\mathbf{v},$$

$$\nabla \cdot (H_T(\mathbf{x}, t)\mathbf{v}) = -\frac{\partial h_T(\mathbf{x}, t)}{\partial t}, \tag{1}$$

where $\mathbf{v}$ is the horizontal velocity vector; p the pressure; $f = f_0 + \beta y$ the Coriolis parameter in a β-plane approximation with y the latitude and f_0 the Coriolis parameter at $y = 0$; ∇ the two-dimensional gradient operator; E_h and E_{υ} are horizontal and vertical (turbulent) friction coefficients; ρ_0 is the constant density; g the gravitational constant; t is time; $z = -H_T(\mathbf{x}, t)$ is the depth of the fluid measured from the rigid upper lid or the resting free surface; $H_T(\mathbf{x}, t) = H(\mathbf{x}) + h_T(\mathbf{x}, t)$ is the total depth of the water column; $\mathbf{F}(\mathbf{x}, t)$ and $h_T(\mathbf{x}, t)$ are *prescribed* forcing terms, $\alpha = \frac{1}{2}$ when there is a free surface and $\alpha = 1$ when there is a rigid lid and $\delta_E = (E_{\upsilon}/f_0)^{1/2}$ the Ekman layer thickness (cf. Pedlosky 1987; Power et al. 1989). The forcing term h_T is included in anticipation of a possible laboratory forcing mechanism in which motion of a profiled upper lid forces the flow. The forcing vector $\mathbf{F}$ is either a wind forcing or a prescribed Ekman-induced velocity profile $\upsilon_T(\mathbf{x}, t)$ associated with a rigid lid; that is, $\mathbf{F}(r, \theta, t) = \boldsymbol{\tau}/[\rho_0 H_T(\mathbf{x}, t)]$ or $f\delta_E \mathbf{v}_T(\mathbf{x}, t)/[2H_T(\mathbf{x}, t)]$ for wind or lid-driven Ekman-induced forcing, respectively, with windstress $\boldsymbol{\tau}$.

After linearization these are Laplace's tidal equations (LTE) in the zero rotational Froude number limit [for typical length scale L and average depth $\overline{H}$ the rotational Froude number $f^2 L^2/(g\overline{H}) \rightarrow 0$] or constrained by a rigid lid; *free* surface undulations are therefore absent. The topographic profile under consideration consists of an interior ocean and a shelf, both of constant depth, and an abrupt shelf break at radius $r = R_s$:

$$H(\mathbf{x}) = (H_2 - s_2 y)\Theta[R_s - r] + (H_1 - s_1 y)\Theta[r - R_s], \tag{2}$$

with Heaviside function $\Theta[\ \cdot\ ]$. Two scenarios are anticipated: (i) an ocean with $\beta = \beta_0$ and no slopes $s_1 = s_2 = 0$ or (ii) a laboratory equivalent with $\beta = 0$ and $s_1/H_1 = s_2/H_2 = \beta_0$. The domain for laboratory scenario (ii) is sketched in Fig. 1 🔵. Both scenarios are identical at leading order in s_1, s_2 and hereafter we consider only scenario (i). Step shelf topography obviously is a convenient mathematical idealization that can lead to nonhydrostatic and ageostrophic effects in three-dimensional flows. This will be discussed further in section 5.

Vorticity dynamics arises from (1):

$$\frac{\partial \xi}{\partial t} + J\left(\Psi, \frac{f + \xi}{H_T(\mathbf{x}, t)}\right) + \nabla \cdot \left(\frac{f + \xi}{H_T(\mathbf{x}, t)}\nabla\chi\right)$$

$$= \mathbf{k} \cdot \nabla \times \mathbf{F} - \alpha\delta_E \nabla \cdot \left(\frac{f}{H_T(\mathbf{x}, t)^2}\nabla\Psi\right)$$

$$- \alpha\delta_E J\left(\frac{f}{H_T(\mathbf{x}, t)^2}, \chi\right) + E_h \nabla^2 \xi, \tag{3}$$

$$\xi = \nabla \cdot \left(\frac{1}{H_T(\mathbf{x}, t)}\nabla\Psi\right) - J\left(\chi, \frac{1}{H_T(\mathbf{x}, t)}\right),$$

$$\nabla^2 \chi = -\frac{\partial h_T}{\partial t}, \tag{4}$$

where a Helmholtz momentum vector decomposition

$$H_T(\mathbf{x}, t)\mathbf{v} = \mathbf{k} \times \nabla\Psi + \nabla\chi \tag{5}$$

introduces a transport streamfunction Ψ with associated vorticity ξ and a velocity potential χ. No flow normal at $r = R$ gives $\Psi = 0$, $\partial\chi/\partial r = 0$, and no-slip gives $\mathbf{n} \cdot \nabla\Psi = \partial\Psi/\partial r = 0$, where $\mathbf{n}$ is the outward normal at $r = R$.

Nondimensionalization by R and f_0 with $t = t'/f_0$, $\beta = \beta' f_0/R$, $\{\Psi, \chi\} = \{\Psi', \chi'\}R^3 f_0$, $\xi = \xi' f_0$, $h_T = \Delta h h'_T$ yields (after omission of the primes)

$$- \mu r'(r, \theta, t) - \alpha \kappa \nabla \cdot \left(\frac{}{H_T(\mathbf{x}, t)^2} \nabla \Psi \right)$$

$$- \alpha \kappa J \left(\frac{f}{H_T(\mathbf{x}, t)^2}, \chi \right) + \frac{1}{Re} \nabla^2 \xi, \qquad (6)$$

$$\xi = \nabla \cdot \left(\frac{1}{H_T(\mathbf{x}, t)} \nabla \Psi \right) - J \left(\chi, \frac{1}{H_T(\mathbf{v}, t)} \right),$$

$$\nabla^2 \chi = -\gamma \frac{\partial h_T}{\partial t}, \qquad (7)$$

with forcing $F^\dagger$ and a forcing number $\mu \equiv \tau_0/[f^2{}_0 R^2 \rho_0]$ or $\kappa \Delta\Omega^*/f_0$ for wind- or Ekman-induced forcing, respectively; Ekman number $\kappa \equiv \delta_E/(R) = (E_\mathbf{v}/(f_0 R^2))^{1/2}$;Reynolds number $Re \equiv f_0 R^2/E_h$; $\gamma = \Delta h/R$; and $\Delta\Omega^* = f_0 \Delta\Omega$ is a typical amplitude of the curl of forcing.

Inviscid modes of the linearized system (6)–(7) with $\mu = \kappa = 1/Re = 0$ are studied in section 3. Forced–dissipative linear responses of (6)–(7) are studied in section 4.

3. Linear inviscid modes

In absence of forcing (i.e., with $h_T = F^\dagger = 0$ and $\nabla \chi = 0$), dissipation and nonlinearity (6)–(7) reads

$$\frac{\partial}{\partial t} \nabla \cdot \left(\frac{1}{H(\mathbf{x})} \nabla \Psi \right) + J \left(\Psi, \frac{1 + \beta y}{H(\mathbf{x})} \right) = 0. \qquad (8)$$

Given profile (2), separate shelf and interior β-plane vorticity dynamics along with streamfunctions Ψ_1 and Ψ_2, respectively, are found on either side of the shelf break and are linked by continuity and matching conditions at the shelf break:

$$\frac{\partial \nabla^2 \Psi_j}{\partial t} + \beta J(\Psi_j, y) = 0 \qquad \text{with } j = 1, 2; \qquad (9)$$

$$\Psi_1 = 0 \qquad \text{at } r = R; \qquad (10)$$

$$\Psi_1 = \Psi_2; \qquad (11)$$

and

$$\frac{\partial_2 \Psi_1}{\partial t \partial r} - \frac{H_1}{H_2} \frac{\partial^2 \Psi_2}{\partial t \partial r} - (1 + \beta y) \frac{(H_2 - H_1)}{R_s H_2} \frac{\partial \Psi_2}{\partial \theta} = 0$$

$$\text{at } r = R_s. \qquad (12)$$

The matching condition follows by radial integration of (8) over an infinitesimally small interval across the shelf break.

a. Asymptotic limits

When $\beta = 0$ system (9)–(12) admits cylindrical shelf-wave solutions

$$\sum_{m=-\infty}^{\infty}{}' \cdots_m \left(\frac{}{R_s}\right) \cdots \qquad (14)$$

(the prime denotes that $m = 0$ is excluded in the summation) with disperion relation

$$\omega_m = \frac{(H_2 - H_1)\left[\left(\dfrac{R_s}{R}\right)^m - \left(\dfrac{R_s}{R}\right)^{-m}\right]}{H_2\left[\left(\dfrac{R_s}{R}\right)^m + \left(\dfrac{R_s}{R}\right)^{-m}\right] - H_1\dfrac{|m|}{m}\left[\left(\dfrac{R_s}{R}\right)^m - \left(\dfrac{R_s}{R}\right)^{-m}\right]}.$$

(15)

For $f_0 > 0$ (Northern Hemisphere) shelf modes always propagate counterclockwise around the basin: they lean to their right onto the topography. When $m \rightarrow \infty$, (dimensional) shelf-mode frequencies tend to $|\omega^*_m/f_0| \rightarrow (H_2 - H_1)/(H_1 + H_2)$, which is the frequency arising from (8) on an infinite plane with straight step shelf topography. In the oceans H_1 typically is an order of magnitude smaller than H_2 and shelf modes are then near-inertial modes for large $|m|$.

When $H_1 = H_2 = H$ and $\beta \neq 0$ Rossby-mode solutions

$$\Psi = \sum_{l=1}^{\infty} \sum_{m=-\infty}^{\infty} b_m J_m(k_{lm}r)$$

$$\times \exp\left[i\left(m\theta + \frac{\beta}{2\omega_{lm}}r\cos\theta + \omega_{lm}t\right)\right] \quad (16)$$

arise with dispersion relation

$$\omega_{lm} = \pm\frac{\beta}{2k_{lm}} \qquad (17)$$

in which total wavenumber k_{lm} is quantized, that is, determined by the zeroes of the Bessel function of the first kind of order m: $J_m(k_{lm}R) = 0$.

Rossby- and shelf-mode (circles and crosses respectively) dispersion diagrams [graphing (15) and (17)] of frequency versus azimuthal mode number m are joined in one diagram, Fig. 2 ⊙ (I), for oceanic parameter values $R^* = 1500$ km, $R^*_s = 1450$ km, $H^*_1 = 300$ m, $H^*_2 = 3000$ m (when confusion arises dimensional asterisk variables are used),

$$\beta = \frac{R^*\beta^*}{f_0} = \frac{1500 \text{ km} \times 2.0 \times 10^{-11} \text{ m}^{-1} \text{ s}^{-1}}{10^{-4} \text{ s}^{-1}} = 0.3,$$

(18)

and in Fig. 2 ⊙ (II) for laboratory parameter values $R^* = 0.17$ m, $H_1 = 0.3$, $H_2 = 0.6$, $\beta = 0.4$ ($H^*_i = H_i R^*$). Only maximum Rossby-mode frequencies k_{0m} are shown. This shows that for fairly realistic parameter values both separate Rossby- and shelf-mode frequencies slightly overlap, in which case hybrid Rossby–shelf modes are expected to exist.

Instantaneous shelf-mode streamfunction fields for azimuthal mode numbers $m = 1, \cdots, 6$ are displayed in Fig. 3 ⊙, corresponding to the laboratory parameter values in Fig. 2 ⊙ (II); hereafter closed contours denote positive and dashed-dotted contours negative fields. The shelf break will always be indicated by a dotted circular curve. In the upper-right corner of each panel corresponding m values appear. Shelf modes travel counterclockwise around a Northern Hemispheric domain with a time-independent radial structure.

Instantaneous Rossby-mode streamfunction fields, $J_m(k_{lm}) \cos(m\theta + k_{lm}x)$, for the eight smallest k_{lm} values are displayed in Fig. 4 ⊙ corresponding to the laboratory values of Fig. 2 ⊙ (II); in the upper-right corner of each panel corresponding m values appear. Naturally these Rossby modes travel from east to west (here, right to left) through the cylindrical domain. Due to the complexity it is more illuminating to display instantaneous streamfunction fields rather than cotidal and corange lines (i.e., amplitude and phase).

Calculation of free modes for $\beta \neq 0$ and $H_1 \neq H_2$ is more complicated because the linear modal problem is not separable. To investigate the hybrid Rossby–shelf mode nature we followed two solution strategies. First, we solve the linear wave equation (8) separately on shelf and in interior regions in terms of Rossby-mode-type basis functions; matching conditions at the shelf break $r = R_s$ then yield a one-dimensional nonlinear eigenvalue problem for the quantized eigenvalues k and corresponding eigenmodes, which can be solved numerically. Alternatively, we discretize the linear wave equation (8) via finite elements (FEM) and solve the corresponding two-dimensional generalized eigenvalue problem numerically. Fundamentals of the mode-matching approach follow shortly while details on the finite element discretization are found in appendix B. The advantage of the semianalytical strategy is a reduction of dimensionality of the eigenvalue problem, which enhances computational speed and allows more coverage of parameter space $\{R_s, H_1, H_2, \beta\}$, while the advantage of the two-dimensional numerical strategy is that it extends more readily to forced–dissipative regimes. Both approaches provide a consistency check on each other.

b. Dispersion of inviscid hybrid modes

Assuming $\Psi_i \sim e^{i\omega t}$ basis functions solving (9)–(11) on the shelf (Ψ_1) and in the interior (Ψ_2) appear

$$\Psi_1 \sim \sum_{m=-\infty}^{\infty} a_m J_m(kR_s)(J_m(kr)Y_m(kR) - J_m(kR)Y_m(kr))$$

$$\times \exp\left[i\left(m\theta + \frac{\beta}{2\omega}r\cos\theta + \omega t\right)\right],$$

$$\Psi_2 \sim \sum_{m=-\infty}^{\infty} a_m J_m(kr)[J_m(kR_s)Y_m(kR) - J_m(kR)Y_m(kR_s)]$$

$$\times \exp\left[i\left(m\theta + \frac{\beta}{2\omega}r\cos\theta + \omega t\right)\right] \qquad (19)$$

with Bessel function of the second kind Y_m and with frequency ω given by

$$\omega = \pm\frac{\beta}{2k}. \qquad (20)$$

Substitution of (19)–(20) into (12) yields a nonlinear eigenvalue problem

$$\sum_{m=-\infty}^{\infty} A_{mn}(k; R_s, R, H_1, H_2, \beta)a_n e^{im\theta} = 0, \qquad (21)$$

in which matrix A_{mn} is bandlimited, $n = m - 2, \cdots, m + 2$ and a (nonlinear) function of the unknown radial "wavenumber" k. The zeroes of the determinant of matrix $\mathbf{A}$ in (21) for each $\pm\omega$ determine the quantization of k. After truncation of the azimuthal modes to $m = -N, \cdots, N$ the determinant of $\mathbf{A}$ can be approximated via recursion relations for band-limited matrices with two super- and subdiagonals after which the zeroes k_l follow. Notice that $\mathbf{A}$ is then either real or imaginary but not complex: in the absence of dissipation, the frequency ω can be shown to be real from the orthogonality relations in section 3d. Details on the numerical recursion procedure are provided in appendix A.

Neither m nor k are appropriate wavenumbers since hybrid Rossby- and shelf-mode characteristics render the linear problem inseparable; to demonstrate the merging of modes we therefore plot frequency ω_l versus shelf break radius R_s.

Using the semianalytical approach with $N = 16$ Rossby-mode basis functions ($|m| \leqslant 16$), we show ω versus $R_s \in [0.0, 1.0]$ in Fig. 5 for (I) ocean ($\beta = 0.3$) and (II) laboratory ($\beta = 0.4$) parameter values. First, consider selected pure shelf-mode (dashed-dotted lines) and pure Rossby-mode (dotted lines) frequencies versus shelf break radius R_s in Fig. 5a (I). Naturally, pure Rossby-mode frequencies display no R_s dependence. Second, in Fig. 5b (I) the heavy solid lines of the hybrid modes are added, indicating the frequency dependence on R_s. Similar figures appear in Fig. 5 (II) for the laboratory case, where pure Rossby- and shelf-mode branches intersect, hybrid modes in the coupled system emerge as osculations of pure Rossby- and shelf-mode branches, which do not intersect another, as amplification around $R_s = R$ confirms. Near $R_s = R$ hybrid modes alternatingly follow pure shelf-mode and pure Rossby-mode branches more closely (see Fig. 6). Although the dependence of frequency on R_s appears to be symmetrical around $R_s = 0$ small numerical differences in the absolute values are present. Accordingly, detailed expressions of the jump condition at the shelf break

(appendix A) also do not seem to reveal this apparent symmetry. Enlargement of frequency dependence on R_s for narrow shelf widths is shown in Fig. 6. The correspondence between FEM calculations (see appendix B) and the pseudoanalytical method is good (see also Figs. 15, 16). Further improvements may be found by refinement of the resolution. Truncation to $N = 32, 48$ yields improvements for the higher shelf modes while at intermediate frequencies convergence has already set in for truncation to $N = 16$ (see comments in appendix A).

Instantaneous streamfunction fields corresponding to 16 selected eigenfrequencies (starting with "shelf" mode $m = 8$) are shown in Fig. 7 for case (I) $R_s = 0.95, \beta = 0.3$, (II) $R_s = 0.94, \beta = 0.4$. In the first six panels in Fig. 7 (I) and the first four in Fig. 7 (II) the shelf-mode signature is still clearly visible (cf. Fig. 3). The β effect leads to broader shelf-trapped circulation cells in the northern part of the domain: for fixed frequency and fixed depth difference an increase (decrease) in $f = f_0 + \beta y$ yields a smaller (larger) azimuthal mode number (treating m temporarily as continuous). These modes remain nevertheless trapped over the shelf. In Figs. 7g (I) and 7e (II) a marked change sets in for "shelf" mode (I) $m = 2$ and (II) $m = 4$: the northern circulation cell is no longer trapped to the boundary but has obtained a Rossby-mode k_{00} signature. This does not come as a surprise when we notice that the pure, unperturbed Rossby-mode k_{00} frequency has been approached in Fig. 6. Similar behavior is found in Figs. 7g,i (I) and in 7e–g (II) for the original pure shelf modes with $m = 2, 1$. The remaining fields for lower frequencies are merely Rossby modes largely confined to a deep interior ocean with a weak tail over the shelves; that is, the quantization is at leading order determined by the zeroes of $J_m(kR_s)$.

In order to understand the hybrid mode characteristics and demarcate them relative to the complicated high wavenumber Rossby modes, selected hybrid Rossby–shelf modes are followed over one period in Fig. 8 for the panels Figs. 7g,i (I) and 7e–g (II), that is, "shelf modes" (I) $m = 2$, (II) $m = 2, 3, 4$. These modes correspond to the encircled values in Fig. 6. In particular, modes $m = 2, 3, 4$ in Figs. 8e–g (II) vividly demonstrate the hybrid Rossby–shelf mode dynamics: the large deep interior-ocean circulation cells propagate westward as Rossby modes to the western boundary where they transform into shelf modes propagating counterclockwise along and trapped to the shelf break to the eastern boundary where a shelf-wave circulation cell separates from the boundary and changes into a deep interior-ocean Rossby mode again. Of course, for each circulation cell this process takes m eigenperiods since the angular phase speed is roughly, based on the shelf-mode characteristics, ω/m. Mode (II) $m = 2$ in effect has some Rossby-mode k_{10} characteristics that naturally correspond to its location in Fig. 6 (II).

Although our calculations are in a closed basin without an equator, the southern shelf-mode guide may be envisaged qualitatively as the equatorial Kelvin waveguide after allowing for surface undulations.

Dorr and Grimshaw (1986) analyzed the inviscid system (8) for smooth shelf topography $H(\mathbf{x})$, shallow on the shelf and exponentially tapering to a constant deep interior-ocean depth, in a semi-infinite basin with straight coast line. Assuming a long-wave limit and with $\beta = O(\epsilon)$ they recognized three regimes, scaling the equations with f_0 and a length scale typical of the topographic shelf width and introducing a longshore wavenumber m: (i) $\omega = O(1)$, $m = O(1)$; (ii) $\omega = O((\epsilon)^{1/2})$, $m = O((\epsilon)^{1/2})$; and (iii) $\omega = O(\epsilon)$, $m = O(\epsilon)$ ($\epsilon \ll 1$). Via a WKB-type analysis and matching the shelf solution to deep interior Rossby solutions they found that in regime (i) shelf waves remain trapped since the frequency is too large to allow Rossby wave radiation, in regime (ii) shelf waves are trapped at low latitudes but radiate into Rossby waves at high latitudes, and in regime (iii) shelf waves radiate into Rossby waves at all latitudes. Dorr and Grimshaw (1986) derived a critical turning latitude for regime (ii),

$$\frac{2\omega^2}{|f_0 c_0|} = \gamma \, \text{sgn}(f_0) + \sqrt{\beta^2 + \gamma^2}, \qquad (22)$$

where c_0 is the long-wave phase speed, and β and γ are derivatives of f in alongshore and offshore directions. Heuristically, we can expect this radiation into Rossby waves: for fixed frequency ω the maximum Rossby-mode frequencies are determined; when ω is close to or below these maximum frequencies, shelf waves will have higher azimuthal mode number and smaller circulation cells in the south since for fixed ω smaller f-values at low latitudes yield larger m values and vice versa, while traveling to higher latitudes the circulation cells grow until they match the corresponding Rossby-mode circulation cells and travel to the west like Rossby waves. Rossby modes impinging on boundaries undergo the opposite sequence. Alternatively, for $\omega = \beta/(2k)$ a smaller total wavenumber k in the northern domain yields larger Rossby wave frequencies, which at a certain critical latitude, that is, critical value of f, matches the shelf wave frequency and radiation or absorption of Rossby waves takes place. Notice that this long-wave modal behavior is reversed relative to hybrid Kelvin–Rossby modes (Grimshaw and Allen 1988), where the Kelvin wave is trapped at high latitudes and radiates or absorbs Rossby waves at low latitudes.

Figures 5, 6, and 7 show that three regimes can indeed be recognized when $R - R_s = O(\epsilon)$, for example, consider (I) $R_s = 0.95$, and (II) 0.94, respectively, in Fig. 6. The corresponding eigenmodes are (i) trapped like shelf modes in Figs. 7a–f (I) and 7a–d (II); (ii) radiate into Rossby waves in Figs. 7g,i (I) and 7e–g (II); but regime (iii) seems to be defined by Rossby modes that live mainly in the deep interior ocean, and the correspondence with Dorr and Grimshaw's (1986) theory is less clear. In contrast to the one dispersion curve for step shelf topography, multiple radial branches occur in the dispersion diagram for smooth shelf topography. Each higher-order branch has lower frequencies for fixed alongshore wavenumber and will for small alongshore wavenumbers eventually overlap with Rossby wave frequencies. Dispersion for a shelf with flat flanks connected with a linear slope is shown as an example in Fig. 9. The above may explain why regime (iii) exists for smooth profiles and not for the step shelf profiles. Notice that our analysis extends Dorr and Grimshaw's analysis, albeit for specific topography and domain shape, by providing the global eigenmode analysis for

an entire ocean basin, which sheds new light on the hybrid shelf–Rossby mode characteristics.

c. Particle paths

Generally velocity fluctuations at a point differ from the mean velocity at that point. In particular, the mean Eulerian velocity $\mathbf{U}_E$ at a point is different from the mean Lagrangian velocity $\mathbf{U}_L$ of a marked fluid particle and it is the latter that characterizes the mass transport, mass being conserved on a fluid particle in the absence of friction and forcing. The velocity of a particle moving from position $\mathbf{x}_0$ at time t_0 to $\mathbf{x}$ at time t is

$$\mathbf{u}(\mathbf{x}, t) = \mathbf{u}(\mathbf{x}_0, t) + \Delta\mathbf{x} \cdot \nabla \mathbf{u}(\mathbf{x}_0, t). \quad (23)$$

Upon approximating $\Delta\mathbf{x}$ by $\int_{t_0}^{t} \mathbf{u}(\mathbf{x}_0, t)\, dt$, rearranging and time-averaging (23) over one wave period (indicated by angle brackets $\langle \cdot\ \cdot\ \rangle$), one derives the well-known relation that the Lagrangian velocity is the sum of the Eulerian velocity and a Stokes drift $\mathbf{U}_S$ (cf. Longuet-Higgins 1969):

$$\mathbf{U}_L - \mathbf{U}_E = \mathbf{U}_S \equiv \left\langle \int_{t_0}^{t} dt\, \mathbf{u}(\mathbf{x}_0, t) \cdot \nabla\mathbf{u}(\mathbf{x}_0, t) \right\rangle. \quad (24)$$

Moore (1970) showed for the LTE that

$$(U_L H)_x + (V_L H)_y = 0, \qquad (U_L \partial_x + V_L \partial_y)\left(\frac{f}{H}\right) = 0. \quad (25)$$

When there are no closed geostrophic contours f/H this implies that $\mathbf{U}_L = 0$ and also that $\mathbf{U}_S = -\mathbf{U}_E$. In particular, the Stokes drift is equal and opposite to the mean Eulerian velocity for pure Rossby waves in a flat-bottom basin. In these cases no net mass transport is induced by the linear wave motion. This conclusion is altered for topographic shelf profiles with closed geostrophic contours for which wave-induced mass transport does emerge.

Particle trajectories form another way to distinguish the hybrid modes from the ones of pure β-plane Rossby and pure topographic shelf waves. At the linear, small amplitude level of approximation it is consistent to linearize the dynamical system for fluid particles, that is,

$$\frac{dr}{dt} = -\frac{1}{rH(\mathbf{x})}\frac{\partial\Psi}{\partial\theta},$$

$$\frac{d\theta}{dt} = \frac{1}{rH(\mathbf{x})}\frac{\partial\Psi}{\partial r}, \qquad\qquad (26)$$

around their initial condition $\{r_0(t), \theta_0(t)\}$ and the leading-order harmonic behavior follows immediately from a Taylor series expansion of $\Psi = A\Psi^{(0)} + A^2\Psi^{(1)} + \cdots$ (in amplitude A). The next order contribution leads to a net drift of the fluid particles, the Stokes drift (e.g., Lighthill 1993). Such direct calculations of the Stokes drift from the particle paths is of course equivalent to (24), although in polar coordinates one should remember that

$$V_s = \left\langle r\frac{d\theta}{dt} \right\rangle. \qquad\qquad (27)$$

We will calculate the harmonic particle oscillations, the Stokes drift, and integrate (26) numerically. This numerical integration provides a better indication of the local linear particle trajectories but any observed particle drift based on the linearized solution $\Psi^{(0)}$ to the wave equation only is of course incomplete under absence of potential $O(A^2)$ advective contributions stemming from $\Psi^{(1)}$.

Given an initial condition $\{r_0, \theta_0\}$ particle trajectories for shelf-mode solutions are calculated from streamfunction [cf. (13)–(15)]:

$$r > R_s, \quad (28)$$

$$\Psi_2 = A_m \left(\frac{r}{R_s}\right)^{|m|} \cos(\omega_m t + m\theta + \alpha_m), \qquad r < R_s, \quad (29)$$

with $\omega_m < 0$, phase α_m, and $m > 0$. A leading-order Taylor expansion of (26) and (28)–(29) yields harmonic particle trajectories (see appendix C). These harmonic solutions constitute ellipses in $\{r, \theta\}$ space. Starting initially on the shelf particle motion is clockwise and starting initially in the deep interior ocean it is counterclockwise around the focal points of each ellipse. Notice that both radial and azimuthal velocities are discontinuous and a trajectory traversing the shelf break will be continuous and will contain a kink; notice also that this is not reflected in the linearized, leading-order particle motion. Azimuthal velocities are opposite on and off the shelf. Continuing to higher order while using the leading-order solution into the next-order contribution, a counterclockwise Stokes drift is obtained in the azimuthal direction only:

$$\theta_S = -\frac{A_m^2}{2\omega_m}\left(mf_\theta^2(r_0) + \frac{df_\theta(r_0)}{dr}f_r(r_0)\right), \qquad (30)$$

which is quadratic in A_m and $\theta_S > 0$ for $r_0 \neq R_s$. However, a Taylor series expansion is inappropriate across an abrupt shelf break where a delta function hampers the ordering. Longuet-Higgins (1969) calculated the Stokes drift for a smooth topographic shelf profile, a tanh profile, which tends to uniform shallow and open ocean depths, and finds, via a general expression, that the total integrated Stokes drift, over depth and across the shelf, is opposite to the direction of wave propagation, that is, clockwise. Consequently there is a region sandwiched between the extremes of shallow and deep water where the Stokes drift is clockwise and in the limit when the smooth tanh profile becomes a step, this region narrows, ultimately giving rise to a delta function overpowering the counterclockwise Stokes drift on the flat-bottom flanks. Indeed, inspection of df_θ/dr reveals a contribution,

$$-\frac{A_m^2 f_r(r)}{2\omega_m R_s}\left|\frac{m}{RH_1}\frac{\left(\frac{R_s}{R}\right)^{m-1} + \left(\frac{R_s}{R}\right)^{-(m+1)}}{\left(\frac{R_s}{R}\right)^m - \left(\frac{R_s}{R}\right)^{-m}} - \frac{|m|}{R_s H_2}\right|$$

$$\times \, \delta(r - R_s) < 0, \qquad (31)$$

that is negative at $r_0 = R_s$, and the Stokes drift (30) right at the shelf break is thus clockwise, that is, opposite to the direction of wave propagation.

The complete solution of (26), using a linear eigenmode as streamfunction, can in principle be found by going to a moving frame such that Ψ becomes time-independent and by applying Hamilton–Jacobi theory. Instead of Hamilton–Jacobi's approach, which will be involved and contain subtleties due to the abrupt shelf break, we will numerically integrate (26)–(29) with an explicit fourth-order Runge–Kutta scheme. The leading-order linear particle motion and the complete trajectory in a frame rotating with $\frac{1}{2}f_0$ are shown in the two panels of Fig. 10 ⊙ (i) for the $m = 4$ laboratory shelf mode [i.e., parameter values as in Fig. 7 ⊙ (II)]. The amplitudes of the ellipses on the shelf have been scaled down relative to ones in the interior for display purposes. In a frame of reference moving with additional angular phase speed $c = \omega/m$ trajectories in Fig. 10b ⊙ (i) become the ones shown in Fig. 11 ⊙.

Particle trajectories for pure Rossby modes and hybrid Rossby–shelf modes can be presented in a united format with streamfunction

$$\Psi = A_l \sum_m \phi_{ml}(k_l r) \cos\left(m\theta + \frac{\beta}{2\omega_l}r\cos\theta + \omega_l t + \gamma_{lm}\right). \qquad (32)$$

For a Rossby mode the summation includes only one value of m, $\Phi_{ml} = J_m(k_l r)$ (for given m, $k_l \equiv k_{lm}$), and phase $\alpha_{lm} = \alpha_m$ [cf. (16)]. For a hybrid Rossby–shelf mode m runs from $-\infty, \cdots, \infty$;

$$\phi_{ml} = |a_{ml}| \begin{cases} J_m(k_l R_s)[J_m(k_l r)Y_m(k_l R) - J_m(k_l R)Y_m(k_l r)], & r > R_s \\ J_m(k_l r)[J_m(k_l R_s)Y_m(k_l R) - J_m(k_l R)Y_m(k_l R_s)], & r < R_s; \end{cases} \qquad (33)$$

phase $\gamma_{lm} = c_l + \alpha_{ml}$ with $\cos\alpha_{ml} = \mathrm{Re}(a_{ml})/|a_{ml}|$, $\sin\alpha_{ml} = \mathrm{Im}(a_{ml})/|a_{ml}|$; and A_l, c_l are arbitrary amplitude and phase [cf. (19)]. The harmonic particle trajectories arising at leading order in A_l are found in appendix C.

The Stokes drift for Rossby modes is

$$U_S = \frac{A_l^2}{2\omega_{lm}r_0 H_2}\cos\theta_0 k_{lm}^2 J_m'(k_{lm}r_0)J_m(k_{lm}r_0),\qquad(34)$$

$$V_S = r_0\dot\theta_S - \frac{1}{2}\frac{A_l^2}{\omega_{lm}r_0^2 H_2}k_{lm}J_m'(k_{lm}r_0)J_m(k_{lm}r_0)$$

$$\times\left(m - \frac{\beta}{2\omega_{lm}}\sin\theta\right)$$

$$= \frac{1}{2}\frac{A_l^2}{\omega_{lm}r_0 H_2}\left\{\left(-m + \frac{\beta}{2\omega_{lm}}\sin\theta\right)\right.$$

$$\times k_{lm}^2[J_m'^2(k_{lm}r_0) + J_m''(k_{lm}r_0)J_m(k_{lm}r_0)]$$

$$\left.+ k_{lm}^2\sin\theta J_m'(k_{lm}r_0)J_m(k_{lm}r_0)\right\},\qquad(35)$$

which may also be verified against (24) and is again a second-order quantity in A_l. A similar but more involved expression arises for hybrid Rossby–shelf modes that includes a delta function contribution due to the sudden shelf break. The leading-order linear particle motion and the complete trajectory are shown in the two panels of Fig. 10 ◑ (ii) for the first $m = 0$ laboratory Rossby mode [i.e., parameter values as in Fig. 7 ◑ (II)]. The leading-order linear particle motion and the complete trajectory are shown in the two panels of Fig. 10 ◑ (iii) for the $m = 4$ laboratory hybrid Rossby–shelf mode [i.e., parameter values as in Fig. 7 ◑ (II)].

d. Orthogonality, synthesis, and initial value problem

The normal modes of (8) or (9)–(12) satisfy orthogonality relations similar to the ones for shallow water equations (Platzmann 1972; Pratt 1997). The only difference is that a rigid lid eliminates free-surface contributions. With $\Psi = \Sigma_j A_j \varphi^j e^{i\omega_j t}$ the orthogonality relation reads

$$i(\omega_{j_1}^* - \omega_{j_2})\int dA\frac{1}{H}\nabla\varphi^{*j_1}\cdot\nabla\varphi^{j_2} = 0,\qquad(36)$$

in which asterisks denote complex conjugate variables, and contains only terms associated with kinetic energy. When there is no multiplicity, that is, there are no equal frequencies, ω_j is seen to be real. Otherwise, eigenmodes with the same eigenfrequency may still be shown to be orthogonal. For a geostrophic mode $\omega_g = 0$ one derives from (8)

$$\int dA\frac{1}{H}\nabla\varphi^{j^\circ}\cdot\nabla\varphi^g = 0.\qquad(37)$$

Initial value problems can now be solved by projection of initial conditions

$$\Psi(\mathbf{x}, t = 0) = \Psi_0(\mathbf{x}),\qquad(38)$$

onto individual eigenmodes while using the orthogonality relations, thus establishing amplitude and phase of each mode, and subsequent updating of the harmonic contributions in the summation of all eigenmodes.

The synthesis of the nongeostrophic eigenmodes follows by multiplication of (38) by complex conjugates of the eigenmodes and integration over the domain while using (36)–(37):

$$\phi(\mathbf{x}, t) = \sum_j A_j \varphi^j e^{\cdots}, \qquad A_j = \frac{\cdots}{\int dA \frac{1}{H} \nabla \varphi^{j*} \cdot \nabla \varphi^j}. \qquad (39)$$

There is no orthogonality rule for the geostrophic modes and their synthesis has to follow otherwise (cf. Greenspan 1980 and Pratt 1997). Geostrophic contours that intersect the boundary where $\Psi = 0$ do not contribute.

The integrated circulation of φ^j along closed geostrophic contours C_g defined by $J(\Psi_g, (1 + \beta y)/H) = 0$ and with outward normal $\mathbf{n}_C$ reads

$$i\omega \int_{C_g} dl \frac{\mathbf{n}_C \cdot \nabla \varphi^j}{H} = 0, \qquad j > 0, \qquad (40)$$

as is found upon integration of (8). This result is used to determine $\Psi_g \equiv A0\Psi0$:

$$\int_{C_g} dl \frac{\mathbf{n}_c \cdot \nabla \Psi_0}{H} = \int_{C_g} dl \frac{\mathbf{n}_c \cdot \nabla \varphi_g}{H} + \sum_{j=1}^{\infty} \int_{C_g} dl \frac{\mathbf{n}_c \cdot \nabla \varphi^j}{H}$$

$$= \frac{d\varphi_g}{d\eta} \int_{C_g} dl \frac{\mathbf{n}_c \cdot \nabla \eta}{H}, \qquad (41)$$

where $\eta \equiv (1 + \beta y)/H$. Once the streamfunction is fixed on some boundary, for example, at $r = R$, the ordinary differential equation (41) can be solved. When η is constant over a certain area $\mathcal{A}$ of space, conservation of potential vorticity may be invoked from which it follows that the relative vorticity equals its initial value, that is, $\nabla \cdot (\nabla \Psi/H) = \nabla \cdot (\nabla \Psi_0/H)$. In completion of the geostrophic synthesis possible separate solutions in constant f/H areas have to be connected smoothly to a known constant value of Ψ at a boundary.

Geostrophic synthesis was circumvented for the pure shelf-mode initial value problem because it could also be solved directly and without explicit synthesis via Laplace transform methods. Geostrophic synthesis was unnecessary for the pure Rossby mode problem and was automatically included in the finite element calculations we performed for the hybrid Rossby–shelf problem.

Let us consider the initial value problem for the laboratory parameter values. Finite element calculations were used because the synthesis with the pseudoanalytically determined eigenmodes was more cumbersome and appeared to converge rather slowly (using truncations of $N = 16, 32, 48$).

What is the fate of a trapped anomaly at the southern boundary? Focusing on the laboratory case with $R_s = 0.94$, the pure shelf-mode solution (i.e., $\beta = 0$) is shown in Fig. 12 ⊙ (i) in 16 panels, each 20 time units f^{-1}_0 spaced in time; the initial structure is seen to be pulled apart by typical shelf mode dispersion but it is also evident that the dynamics remains trapped near the shelf break—as expected. Turning on β to 0.4 yields entirely different behavior since the initial anomaly projects on shelf modes, Rossby modes, and hybrid Rossby–shelf modes. Using finite elements the sequence in Fig. 12 ⊙ (ii) emerges: the anomaly initially travels counterclockwise northward along the shelf but then radiates into Rossby modes [Fig. 12d ⊙ and further] and a series of deep interior ocean modes subsequently determine the time evolution, although the shelf mode signature remains visible at the southern boundary.

For the same parameter values as above a large axisymmetric anomaly centered in the domain used as initial condition yielded predominantly interior-ocean Rossby mode dynamics with little shelf mode signal.

The amplitudes of the modes versus their frequency for these two initial conditions are displayed in Fig. 13 ⊙ with selected numbers referring to the shelf modes from which they originate and "R" referring to the Rossby mode origin. The boundary-trapped anomaly (Fig. 13a ⊙) projects more significantly onto the hybrid Rossby–shelf modes [cf. Fig. 12 ⊙ (ii)] than the initially axisymmetric anomaly that projects mainly onto the low-frequency Rossby modes (Fig. 13b ⊙). Notice that in the projection spurious numerical modes with high wavenumbers but varying frequency, that is, the ones between the numbered modes, essentially have zero amplitude. Time evolution of transport at the shelf break $r = R_s$ gives a more detailed impression to what extent a shelf-trapped anomaly excites motion off the shelf and, vice versa, to what extent an axisymmetric deep interior-ocean anomaly excites shelf modes. In Fig. 14a ⊙ the signal of Ψ versus the azimuthal angle at the shelf break diminishes in amplitude over time by cancellation of the contribution to each mode over the shelf (in this inviscid calculation the amplitude of each mode is naturally conserved), while in Fig. 14b ⊙ the signal on the shelf increases in time but remains limited. The numbers in Fig. 14 ⊙ correspond to the panels in Fig. 12 ⊙: curve 1 corresponds to $\Psi(R_s, \theta)$ for the initial condition, curve 2 to $\Psi(R_s, \theta)$ 20 time units later, and so forth; curves 1–4 are solid lines, curves 5–7 are dashed, and curves 10, 13, and 16 are dashed-dotted lines.

One expects certain initial conditions to favor hybrid modal behavior when the initial profile displays similar spatial

structure as the separate pure shelf and Rossby modes involved in the encounter.

4. Linear forced–dissipative wave response

In this section the influence of Ekman friction on resonantly excited linear hybrid Rossby-shelf modes is assessed numerically. Forced–dissipative modes can, of course, always be excited by an appropriate forcing structure. This excitation can be made mathematically precise, in the linear regime, by deriving orthogonality principles for the linear forced–dissipative equations. Consequently, equations adjoint to the forced–dissipative equations of motion arise and both sets of equations have to be considered in unison.

The linearized and simplified harmonically forced–dissipative equations without lateral friction read [cf. (6)–(7)]

$$\frac{\partial \xi}{\partial t} + J\left(\psi, \frac{1 + \beta y}{H(\mathbf{x})}\right) + \nabla \cdot \left(\frac{1 + \beta y}{H(\mathbf{x})}\nabla\chi\right)$$

$$= \mu F^\dagger(r, \theta, t) - \alpha\kappa\nabla \cdot \left(\frac{(1 + \beta y)}{H(\mathbf{x})^2}\nabla\Psi\right), \quad (42)$$

$$\xi = \nabla \cdot \left(\frac{1}{H(\mathbf{x})}\nabla\Psi\right), \qquad \nabla^2\chi = -\gamma\frac{\partial h_T}{\partial t}, \qquad (43)$$

with forcing $F^\dagger$ and a forcing number $\mu \equiv \tau_0/[f_0^2 R^2 \rho_0]$ or $\kappa\Delta\Omega*/f_0$ for wind- or Ekman-induced forcing, respectively.

Lateral friction has been discarded for simplicity; it is easy to include these frictional effects near the boundary at $r = R$ but it is more complicated to assess the three-dimensional frictional effects on the two-dimensional flow at the shelf break $r = R_s$. Only Ekman damping is therefore included.

The oceanic forced–dissipative response, displayed as forcing frequency σ versus mean absolute amplitude, is calculated for a zonal wind stress forcing depending sinusoidally on only the meridional coordinate, that is, $F^\dagger \sim \sin(2\pi y/R) e^{i\sigma t}$ (with $h_T = 0$). Typical response curves in Fig. 15 ⊙ reveal that in the interval of estimated oceanic values (i) $\kappa = 10^{-5}$, $\mu = 10^{-7}$, (ii) $\kappa = 10^{-5}$, $\mu = 10^{-8}$, and (iii) $\kappa = 10^{-6}$, $\mu = 10^{-7}$; strongly damped and resonant response both occur ($\kappa = \delta_E/R \approx 1.5/(1.5 \times 10^6) = 10^{-6}$ and $\mu = \tau_0/[f_0^2 R^2 \rho_0] \approx 1/(10^{-8} \times 2.25 \times 10^{12} \times 10^3) \approx 10^{-8}$).

The laboratory forced–dissipative response is calculated for the same zonal wind stress, and by a harmonic topographic forcing $h_T = \cos(m\theta) e^{i\sigma t}$, which corresponds to vibrating the upper lid in the prescribed fashion (notice that total volume is preserved). Response curves versus frequency for the sinusoidal windstress case are shown in Fig. 16a ⊙ for $\kappa = 0.0008$, 0.001 65, 0.0033. With viscosity $E_h = \nu = 10^{-6}$ m² s⁻¹, $f_0 = \pi$ s⁻¹, and $R* = 0.17$ m damping $\kappa = 0.0033$ in which case the response is hardly resonant since forcing directly balances damping. For smaller values of κ typical resonant response curves appear in which resonant frequencies are close to the inviscid ones. Topographic forcing is more flexible and easier to realize in the laboratory. Typical response curves are shown in Fig. 16b ⊙ for $\gamma = 0.15$ and κ: (i) 0.000 33, (ii) 0.0001, (iii) 0.000 05, and (iv) 0.000 033. The streamfunction fields corresponding to resonant peaks $m = 1, 2, 3, 4$ numbered in Fig. 16a ⊙ are singled out in Fig. 17 ⊙; comparison with Figs. 7h,g,f,e ⊙ (II) shows the similarities with corresponding inviscid normal modes.

The finite element code with which these calculations are performed is described in appendix B.

5. Summary and discussion

Hybrid (planetary) β-plane Rossby and topographic shelf modes have been studied in detail for a two-dimensional homogenous fluid in a cylindrical basin with axisymmetric step shelf topography and, effectively, rigid lid. Essentials of fluid flow are now reduced to interacting β-plane Rossby, topographic shelf, and hybrid Rossby–shelf modes. In this paper, solely linearized dynamics around a resting state has been investigated in terms of these normal modes. Due to combined β-plane and topographic effects significant changes in modal structure occurred in a frequency interval in which the separate Rossby and shelf mode dispersion curves overlapped—as expected. For typical oceanic and laboratory parameter values such an overlap interval was shown to exist (e.g., Fig. 2 ⊙). Semianalytical mode matching in detail revealed frequency dependence on shelf break radius R_s (Figs. 5 ⊙ and 6 ⊙) as an alternative for classical dispersion diagrams that are no longer attainable due to the inseparable nature of the linear vorticity dynamics. Hybrid Rossby–shelf modes emerge that embrace Rossby-mode westward propagation in the northern interior ocean and trapped, counterclockwise shelf-mode propagation near the southern shelf break and transform smoothly into each other at eastern and western boundaries (Fig. 8 ⊙). Harmonic particle ellipses underscored the increased complexity of hybrid modes, knowledge that might be of importance in analysis of oceanic float data and analysis of dye displacements in laboratory experiments (Fig. 10 ⊙). Solutions of the initial value problem for two initial conditions (one shelf bound and one axisymmetric) indicated the richer

dynamics with exchange of momentum across the shelf break (Figs. 12–14 ◯☞).

   Relative to previous work by Dorr and Grimshaw (1986), our calculations provided basinwide circulation patterns of hybrid Rossby–shelf modes, whereas their calculations were asymptotic and restricted to straight coastlines but involved more general shelf topography. Relative to the inviscid, rectangular basinwide numerical computation of Miller (1986) our calculations in a cylindrical domain could capture more realistic oceanic parameter values and traced the origin of hybrid modes in detailed frequency–shelf break diagrams. Dorr and Grimshaw (1986) examined the longwave limit of hybrid waves. From the dispersion curves of pure Rossby and pure shelf modes (e.g., Fig. 2 ◯☞) it is immediately clear that hybrid modes are always long waves for step shelf topography. In contrast, overlap in frequencies is found both between long Rossby waves and long shelf waves and between long Rossby waves and short shelf waves for smooth shelf topography (which is expected upon inspection of Fig. 9 ◯☞). Dorr and Grimshaw (1986) apparently did not investigate the latter limit asymptotically since in their scaling frequency and alongshore wavenumber have similar magnitude. Some of Miller's (1986) streamfunction fields appear to be hybrid modes that are coupled long Rossby and short shelf modes and that are, opposite to the long-wave case, trapped at high latitudes and radiating at low latitudes. In addition, these short shelf modes have "group velocities" opposite to long shelf modes. In extension of previous work, we performed some forced–dissipative calculations that revealed the sensitivity of resonant responses to Ekman damping for realistic estimates of laboratory and oceanic frictional values. A study of combined frictional and nonlinear effects is left for the future.

   The linear modal analysis employed here hints at the potential richness of transport phenomena between coastal zones and deep interior oceans. Naturally, it is necessary to include nonlinearity in order to allow and assess transport of tracers. In particular, normal modes could be used to analyze transfer of energy between modes in nonlinear inviscid simulations in extension of the linear initial value problems solved in this paper. Such nonlinear simulations may address the question to what extent a (smooth) shelf break acts as a barrier to transport.

   Laboratory experiments in which hybrid Rossby–shelf modes are visualized have been performed. The configuration consists of a rotating tank with a topographic β plane and shelf topography (as sketched in Fig. 1 ◯☞). Forcing is applied by differentially oscillating the upper rigid lid, which may or may not have some undulations attached underneath to match spatial structures of desired hybrid modes. Preliminary results show qualitative agreement but nonlinearity, three-dimensionality, and lateral friction all play a role in laboratory flows. It is crucial to understand and control these effects in order to visualize a forced–dissipative response with flow patterns close to the inviscid ones. Weakly nonlinear calculations, following work by Pedlosky (1965, 1967) are thus in progress; these calculations are analytical for pure Rossby or shelf waves, and semianalytical (by mode-matching of the separate forced–dissipative Rossby mode solutions on and off the shelf) or numerical for hybrid Rossby–shelf modes.

   Mathematically the simplification from three-dimensional flow to hydrostatic, geostrophic flow is subtle. Bartholomeusz (1958) showed that superinertial waves in LTE followed from a small aspect ratio limit of three-dimensional Euler equations. Miles (1974) showed that LTE only yielded the proper (linear) dynamics in a small aspect ratio limit of the Boussinesq equations with fixed constant stratification. Chapman (1982) compared LTE with corresponding three-dimensional Euler equations for straight abrupt shelf topography. The frequency response induced by a spatially uniform, periodic, horizontal velocity in the deep ocean remained close to the two-dimensional dispersion relation for long along-shelf waves but always involved radiation of vertical oscillating gyroscopic waves to infinity, which for higher along-shelf wavenumbers lead to large discrepancies relative to two-dimensional calculations. In line with the Miles (1974) results Chapman (1982) showed also that stratification can restore hydrostatic balance over abrupt shelf topography. Obviously step shelf topography is a mathematically convenient idealization that may, however, lead to distinct ageostrophic or nonhydrostatic effects in the three-dimensional case, at least locally at the shelf break. The extent to which these ageostrophic or nonhydrostatic effects are reduced, relative to a three-dimensional laboratory analogue, under strong rotation, by frictional effects or by smoothing of shelf slopes still remains unclear. It may be of interest to study this omission in our knowledge if we want to understand differences between ocean and laboratory shelf configurations.

   Naturally, many more questions about linear dynamics of coupled coastal and deep ocean models, in which planetary β effects are retained, remain unanswered. These include issues involving refraction of waves around complicated topography, waves in stratified fluids, and equatorial Kelvin waves that connect the western and eastern shelf-wave guide rather than the shelf waves in the presented model.

REFERENCES

   Bartholomeusz, E. F., 1958: The reflection of long waves at a step. *Proc. Cambridge Philos. Soc.,* **54,** 106–118..

   Bokhove, O., and E. R. Johnson, 1997: On hybrid β-plane Rossby and topographic shelf modes. *Proc. 11th Conf. on Atmospheric and Oceanic Fluid Dynamics,* Tacoma, WA, Amer. Meteor. Soc., 206–207..

Brink, K. H., 1991: Coastal-trapped waves and wind-driven currents over the continental shelf. *Annu. Rev. Fluid Mech.,* **23,** 389–412..

Chapman, D. C., 1982: On the failure of Laplace's tidal equations to model subinertial motions at a discontinuity in depth. *Dyn. Atmos. Oceans,* **7,** 1–16..

Dorr, A., and R. Grimshaw, 1986: Barotropic continental shelf waves on a *β*-plane. *J. Phys. Oceanogr.,* **16,** 1345–1358.. Find this article online

Greenspan, H. P., 1980: *The Theory of Rotating Fluids.* Cambridge University Press, 328 pp..

Grimshaw, R., and J. S. Allen, 1988: Low-frequency baroclinic waves off coastal boundaries. *J. Phys. Oceanogr.,* **18,** 1124–1143.. Find this article online

Huthnance, J. M., 1987: Effect of longshore shelf variations on barotropic continental shelf waves, slope currents and ocean modes. *Progress in Oceanography,* Vol. 19, Pergamon, 177–220..

——, 1995: Circulation, exchange and water masses at the ocean margin: The role of physical processes at the shelf edge. *Progress in Oceanography,* Vol. 35, Pergamon, 353–431..

Kelly, K. A., M. J. Caruso, and J. A. Austin, 1993: Wind-forced variations in sea surface height in the northeast Pacific ocean. *J. Phys. Oceanogr.,* **23,** 2392–2411.. Find this article online

——, R. C. Beardsley, R. Limeburner, K. Brink, J. D. Paduan, and T. K. Chereskin, 1998: Variability of the near-surface eddy kinetic energy in the California curent based on altimetric, drifter, and moored current data. *J. Geophys. Res.,* **103,** 13 067–13 083..

Lamb, H., 1993: *Hydrodynamics.* Cambridge University Press, 738 pp..

Lighthill, J., 1993: *Waves in Fluids.* Cambridge University Press, 504 pp..

Longuet-Higgins, M. S., 1969: On the transport of mass by time-varying ocean currents. *Deep-Sea Res.,* **16,** 431–447..

Miles, J., 1974: On Laplace's tidal equations. *J. Fluid Mech.,* **66,** 241–260..

Miller, A. J., 1986: Nondivergent planetary oscillations in midlatitude ocean basins with continental shelves. *J. Phys. Oceanogr.,* **16,** 1914–1928.. Find this article online

Moore, D., 1970: The mass transport velocity induced by free oscillations at a single frequency. *Geophys. Fluid Dyn.,* **1,** 237–247..

Pedlosky, J., 1965: A study of the time-dependent ocean circulation. *J. Atmos. Sci.,* **22,** 267–272.. Find this article online

——, 1967: Fluctuating winds and the ocean circulation. *Tellus,* **16,** 250–257..

——, 1987: *Geophysical Fluid Dynamics.* Springer-Verlag, 710 pp..

——, 1996: *Ocean Circulation Theory.* Springer-Verlag, 453 pp..

Platzmann, G.W., 1972: Two-dimensional free oscillations in natural basins. *J. Phys. Oceanogr.,* **2,** 117–138.. Find this article online

——, 1984: Normal modes of the world ocean. Part IV: Synthesis of diurnal and semidiurnal tides. *J. Phys. Oceanogr.,* **14,** 1532–1550.. Find this article online

Power, S. B., J. H. Middleton, and R. H. J. Grimshaw, 1989: Frictionally modified continental shelf waves and the subinertial response to wind and deep-ocean forcing. *J. Phys. Oceanogr.,* **19,** 1486–1506.. Find this article online

Pratt, L. J., and S. G. Llewellyn Smith, 1997: Hydraulically drained flows in rotating basins. Part I: Method. *J. Phys. Oceanogr.,* **27,** 2509–2521.. Find this article online

Staniforth, A. N., R. T. Williams, and B. Neta, 1993: Influence of linear depth variations on Poincaré, Kelvin, and Rossby waves. *J. Atmos. Sci.,* **50,** 929–940.. Find this article online

Zienkiewicz, O. C., and R. L. Taylor, 1991: *The Finite Element Method.* 4th ed. McGraw-Hill, 807 pp..

APPENDIX A

6. Numerics 1D Eigenvalue Problem at Shelf Break

Substitution of (19), that is,

$$\sum_{m=-\infty}^{\infty} \cdots \qquad \cdots \qquad \cdots \qquad \left[\left(\cdots \frac{}{2\omega}\cdots\right)\right]. \tag{A1}$$

into the matching condition (12),

$$R_s\left(\frac{\partial^2 \Psi_1}{\partial t \partial r} - \frac{H_1}{H_2}\frac{\partial^2 \Psi_2}{\partial t \partial r}\right) - (1 + \beta y)\left(1 - \frac{H_1}{H_2}\right)\frac{\partial \Psi_2}{\partial \theta} = 0, \tag{A2}$$

yields the following nonlinear eigenvalue problem:

$$\sum_{m=-\infty}^{\infty}\left\{i\frac{1}{2}\,\mathrm{sgn}(\omega)\beta R_s J_m(kR_s)[J'_m(kR_s)Y_m(kR) - J_m(kR)Y'_m(kR_s)]\right.$$

$$-\,i\frac{1}{2}\,\mathrm{sgn}(\omega)\beta\frac{H_1}{H_2}R_s J'_m(kR_s)[J_m(kR_s)Y_m(kR) - J_m(kR)Y_m(kR_s)]$$

$$+\,\frac{1}{2}\beta\left(\frac{H_1}{H_2} - 1\right)R_s\,\cos\theta J_m(kR_s)[J_m(kR_s)Y_m(kR) - J_m(kR)Y_m(kR_s)]$$

$$-\,i(1 + \beta R_s\,\sin\theta)\left(1 - \frac{H_1}{H_2}\right)(m - k\,\mathrm{sgn}(\omega)R_s\,\sin\theta)J_m(kR_s)[J_m(kR_s)Y_m(kR) - J_m(kR)Y_m(kR_s)]\right\}$$

$$\times\, a_m \exp\left[\left(m\theta + \frac{\beta}{2\omega}R_s\,\cos\theta + \omega t\right)\right] = 0, \tag{A3}$$

where the primes indicate derivatives with respect to the argument, $i^2 \equiv -1$ and $\beta/(2\omega) \equiv k\,\mathrm{sgn}(\omega)$. System (A3) may be rewritten as

$$\sum_{m=-\infty}^{\infty}\{iA_m(k)a_{m-2} + B_m(k)a_{m-1} + iG_m(k)a_m + D_m(k)a_{m+1} + iE_m(k)a_{m+2}\}\,\exp[i(m\theta + k\,\mathrm{sgn}(\omega)R_s\,\cos\theta + \omega t)] = 0, \tag{A4}$$

in which coefficients A_m, B_m, G_m, D_m, and E_m are functions of k and depend on parameters R_s, R, H_1, H_2, β. Their definitions are

$$A_m = \frac{1}{4}k\,\mathrm{sgn}(\omega)\beta R_s^2\left(\frac{H_1}{H_2} - 1\right)J_{m-2}(kR_s)[J_{m-2}(kR_s)Y_{m-2}(kR) - J_{m-2}(kR)Y_{m-2}(kR_s)],$$

$$B_m = \frac{1}{2}R_s\left(\frac{H_1}{H_2} - 1\right)\left[\frac{1}{2}\beta + (m - 1)\beta - k\,\mathrm{sgn}(\omega)\right]J_{m-1}(kR_s)\cdot[J_{m-1}(kR_s)Y_{m-1}(kR) - J_{m-1}(kR)Y_{m-1}(kR_s)],$$

$$G_m = \frac{1}{2}\beta\,\mathrm{sgn}(\omega)R_s\left\{J_m(kR_s)[J'_m(kR_s)Y_m(kR) - J_m(kR)Y'_m(kR_s)] - \frac{H_1}{H_2}J'_m(kR_s)[J_m(kR_s)Y_m(kR) - J_m(kR)Y_m(kR_s)]\right\}$$

$$+\left(\frac{1}{2}\mathrm{sgn}(\omega)\beta kR_s^2 - m\right)\left(1 - \frac{H_1}{H_2}\right)J_m(kR_s)\cdot[J_m(kR_s)Y_m(kR) - J_m(kR)Y_m(kR_s)],$$

$$D_m = \frac{1}{2}R_s\left(\frac{H_1}{H_2} - 1\right)\left[\frac{1}{2}\beta - (m + 1)\beta + k\,\mathrm{sgn}(\omega)\right]J_{m+1}(kR_s)\cdot[J_{m+1}(kR_s)Y_{m+1}(kR) - J_{m+1}(kR)Y_{m+1}(kR_s)],$$

$$E_m = \frac{1}{4}k\,\mathrm{sgn}(\omega)\beta R_s^2\left(\frac{H_1}{H_2} - 1\right)J_{m+2}(kR_s)\cdot[J_{m+2}(kR_s)Y_{m+2}(kR) - J_{m+2}(kR)Y_{m+2}(kR_s)]. \tag{A5}$$

The determinant $\mathcal{D}$ of the system

$$iA_m a_{m-2} + B_m a_{m-1} + iG_m a_m + D_m a_{m+1} + iE_m a_{m+2} = 0 \tag{A6}$$

for $m = -\infty, \cdots, \infty$ for each $\pm\text{sgn}(\omega)$ determines the quantization of k (or ω) and can be approximated by truncation to $m = -N, \cdots, N$. Since (A6) has five diagonals, one can recursively compute $\mathcal{D}$ starting from the upper-left corner element G_{-N}. The truncated $\mathcal{D}$ is either real or imaginary depending on the parity of the rank of the truncated system. Renumbering $l = m + N + 1$, the following sequence of recursion relations appears:

$$\mathcal{D}_0 = d_0 = 1,$$

$$\mathcal{D}_1 = id_1 = iG_0',$$

$$\mathcal{D}_2 = d_2 = -(G_1'd_1 + B_1'D_0'), \qquad Z_{22} = d_1, \qquad Z_{12} = B_1' \qquad Z_{21} = D_0'$$

$$($$

$$\mathcal{D}_{2n} = d_{2n},$$

$$d_{2n} = -\{G_{2n-1}'d_{2n-1} + B_{2n-1}'(D_{2n-2}'d_{2n-2} + E_{2n-3}'Z_{(2n-2)(2n-1)}) + A_{2n-1}'(D_{2n-2}'Z_{(2n-1)(2n-2)} - E_{2n-3}'Z_{(2n-2)(2n-2)})\},$$

$$Z_{(2n-1)(2n-1)} = G_{2n-1}'D_{2n-2}' + E_{2n-3}'A_{2n-1}'d_{2n-3},$$

$$Z_{(2n)(2n-1)} = D_{2n-2}'d_{2n-2} + E_{2n-3}'Z_{(2n-2)(2n-1)},$$

$$Z_{(2n-1)(2n)} = B_{2n-1}'d_{2n-2} + A_{2n-1}'Z_{(2n-1)(2n-2)};$$

$$\mathcal{D}_{2n+1} = id_{2n+1},$$

$$d_{2n+1} = \{G_{2n}'d_{2n} + B_{2n}'(-D_{2n-1}'d_{2n-1} + E_{2n-2}'Z_{(2n-1)(2n)}) + A_{2n}'(D_{2n-1}'Z_{(2n)(2n-1)} + E_{2n-2}'Z_{(2n-1)(2n-1)})\},$$

$$Z_{(2n)(2n)} = -G_{2n}'D_{2n-1}' + E_{2n-2}'A_{2n}'d_{2n-2},$$

$$Z_{(2n+1)(2n)} = D_{2n-1}'d_{2n-1} - E_{2n-2}'Z_{(2n-1)(2n)},$$

$$Z_{(2n)(2n+1)} = B_{2n}'d_{2n-1} - A_{2n}'Z_{(2n)(2n-1)},$$

$$(, \qquad\qquad\qquad\qquad\qquad\qquad\qquad\qquad\qquad\qquad\qquad\qquad\text{(A7)}$$

(Click the equation graphic to enlarge/reduce size)

where d_n is the real part of the determinant; $Z_{(n)(n)}$, $Z_{(n-1)(n)}$, $Z_{(n)(n-1)}$ are the cofactors of the lower-right corner, its last column upper neighbor, and its last row left neighbor; $G_l' = G_m'$, etc. The reduction of this determinant recursion for tridiagonal matrices is simpler and only requires knowledge of the previous two determinants.

The zeroes of $\mathcal{D}$ are calculated by an incremental search (Brent's method) through the range of k for constant values of R_s (or β) and zero branches are subsequently followed while incrementally increasing either R_s or β. It is necessary to balance the determinant for large N locally in a small neigborhood of k. For $H_1 = H_2 = H$ the determinant has both single and double zeroes but approximates the analytical Rossby-mode dispersion relation quite well. To speed up the hybrid mode calculations only single zeroes are sought: there are no double zeroes when $H_1 \neq H_2$ and when $\beta \neq 0$.

Once the eigenvalues k are found for both $\pm|\omega|$ the corresponding eigenfunctions are calculated from (A4) for $m = -N, \cdots, N$ by assuming a suitable a_m to be unity and by subsequent inversion. To assure convergence it is necessary to compute both the eigenvalue and the eigenfunction in double precision; even so, precision gets hampered for large values of N due to the small, respectively large, magnitude of J_m and Y_m Bessel functions. Suitable scaling factors were therefore introduced based on the asymptotic envelope of these Bessel functions.

APPENDIX B

7. Weighted Residuals and Finite Elements

Consider the system (42)–(43),

with forcing $F^\dagger = \text{curl}\mathbf{F}$. Multiplication of (B1)–(B2) by test functions ϕ_α, integration over the domain, and expansion of $\Psi = \Sigma\, q_\beta\phi_\beta, \chi = \Sigma\, x_\beta\phi_\beta$ in terms of a truncated sum of (the same) test functions yields the following system of ordinary differential equations:

$$(i\sigma M_{\alpha\beta} + \alpha\kappa K_{\alpha\beta} + S_{\alpha\beta})q_\beta = f_\alpha - D_{\alpha\beta}x_\beta,$$

$$C_{\alpha\beta}x_\beta = i\gamma\sigma h_\alpha, \qquad\qquad \text{(B3)}$$

where

$$M_{\alpha\beta} \equiv \int dA\frac{1}{H(\mathbf{x})}\nabla\phi_\alpha\cdot\nabla\phi_\beta - \int d\mathbf{n}\cdot\phi_\alpha\frac{\nabla\phi_\beta}{H(\mathbf{x})}\bigg|_{r=R},$$

$$K_{\alpha\beta} \equiv \int dA\frac{(1 + \beta y)}{H(\mathbf{x})^2}\nabla\phi_\alpha\cdot\nabla\phi_\beta$$

$$- \int d\mathbf{n}\cdot\phi_\alpha(1 + \beta y)\frac{\nabla\phi_\beta}{H(\mathbf{x})^2}\bigg|_{r=R}$$

$$+ \int dA\frac{\beta}{H(\mathbf{x})^2}\phi_\alpha\nabla y\cdot\nabla\phi_\beta,$$

$$S_{\alpha\beta} \equiv -\int dA\frac{(1 + \beta y)}{H(\mathbf{x})}J(\phi_\alpha, \phi_\beta),$$

$$D_{\alpha\beta} \equiv \int dA\frac{(1 + \beta y)}{H(\mathbf{x})}\nabla\phi_\alpha\cdot\nabla\phi_\beta,$$

$$C_{\alpha\beta} \equiv \int dA\nabla\phi_\alpha\cdot\nabla\phi_\beta,$$

$$f_\alpha = -\int dA\frac{1}{H(\mathbf{x})}\nabla\phi_\alpha\cdot\mathbf{k}\times\mathbf{F}$$

$$+ \int d\mathbf{n}\cdot\phi_\alpha\frac{1}{H(\mathbf{x})}\mathbf{k}\times\mathbf{F}\bigg|_{r=R}. \qquad\qquad \text{(B4)}$$

We have added an extra null term at the boundary to make matrices $M_{\alpha\beta}$ and $K_{\alpha\beta}$ symmetric, and used $\Psi = 0, \mathbf{n}\cdot\nabla\chi = 0$ at $r = R_s$ and continuity and matching conditions at the shelf break for abrupt topography.

In the absence of forcing and dissipation (B3) reduces to the system

$$(i\sigma M_{\alpha\beta} + \kappa K_{\alpha\beta} + S_{\alpha\beta})q_\beta = 0, \text{(B5)}$$

which constitutes a generalized eigenvalue problem and is solved numerically by using LAPACK routines. Since matrix $\mathbf{M}$ is symmetric and $\mathbf{S}$ antisymmetric, forcing frequency σ is guaranteed to be real. Any solution $\Psi = \Sigma\, q_\beta\phi_\beta$ of (B5) now yields a weak solution of (B1)–(B2).

The advantage of the above so-called weighted-residual techniques is that they easily handle abrupt topography. Instead of global basis functions ϕ_α, a natural choice would be Chebychev–Fourier; local basis functions were used that are nonzero only on finite elements (Zienkiewicz and Taylor 1991). These basis functions are linear and based on a decomposition of the domain in triangular elements. Per element there are three different elemental basis functions, each one of unit value at the home node and zero at the others. At these home nodes Ψ, χ thus have values q_β, x_β. Elemental basis functions of unit value at each node constitute together top-hat local basis functions. At the boundaries the triangles have one curved side and the corresponding test functions are first order but slightly more involved. There are no curved elements at the shelf break R_s where the depth $H(\mathbf{x})$ changes abruptly. The finite element grid is uniform in the radial direction except for an optional

refinement at the shelf break and is nonuniform in the azimuthal direction such that the final grid in Cartesian coordinates would be more or less uniform without resolution refinement.

The FEM calculation entailed 3280 elements and 1705 nodes, and the triangular elements were roughly uniform with 128 nodes at the shelf break and 24 radial nodes. The resulting band-limited generalized eigenvalue problem of rank 1577 was solved by LAPACK routines on an HP-9000 computer. Two-dimensional finite element calculations are much slower than the one-dimensional mode-matching approach and the diagrams of frequency versus shelf break radius would have been nearly impossible to achieve. In addition, the discretization introduces numerical dispersion for the higher azimuthal modes since roughly eight nodes are needed per wavelength for a good representation. For the pure shelf-mode problem the numerically calculated frequencies do at first (when there are eight or more nodes per wavelength) approach a constant value, as in the exact solution, but eventually bend down linearly toward zero when approaching the truncation number. This numerical problem hampers the ordering of the frequencies. For the pure shelf modes it suffices to eliminate these high-frequency modes via FFT techniques (at $r = R_s$) but for the coupled system neither FFT techniques nor demarcation

methods based on a numerically defined total wavenumber appear entirely foolproof. Sufficient damping in calculations of the damped resonant response to a harmonic forcing eliminates these spuriously dispersive high-frequency modes, as does projection onto the modes of an initial condition that has no high-wavenumber contributions (cf. Fig. 13 ⊶).

APPENDIX C

8. Harmonic Particle Trajectories

A leading-order Taylor expansion of (26) and (28)–(29) yields harmonic particle trajectories for pure shelf modes:

$$r^{(0)} - r_0 - A_m \frac{f_r(r_0)}{\omega_m} \cos(\omega_m t_0 + m\theta_0 + \alpha_m)$$

$$\equiv r^{(0)} - r_0'$$

$$= -A_m \frac{f_r(r_0)}{\omega_m} \cos(\omega_m t + m\theta_0 + \alpha_m), \qquad \text{(C1)}$$

$$\theta^{(0)} - \theta_0 + A_m \frac{f_\theta(r_0)}{\omega_m} \sin(\omega_m t_0 + m\theta_0 + \alpha_m)$$

$$\equiv \theta^{(0)} - \theta_0' \qquad \text{(C2)}$$

$$= A_m \frac{f_\theta(r_0)}{\omega_m} \sin(\omega_m t + m\theta_0 + \alpha_m)$$

on each side of the shelf, where

$$f_r \equiv \begin{cases} f_{1r} = \dfrac{m}{H_1 r} \dfrac{\left(\dfrac{r}{R}\right)^m - \left(\dfrac{r}{R}\right)^{-m}}{\left(\dfrac{R_s}{R}\right)^m - \left(\dfrac{R_s}{R}\right)^{-m}}, & r > R_s \\[6mm] f_{2r} = \dfrac{m}{H_2 r}\left(\dfrac{r}{R_s}\right)^{|m|}, & r < R_s; \end{cases} \qquad \text{(C3)}$$

$$\left[f_{2\theta} = \frac{\cdots}{H_2 r R_s} \left(R_s \right) \right], \qquad r < R_s.$$

At leading order (26) and (32) with $H = H(r)$ yield the harmonic particle trajectories for the Rossby and hybrid Rossby shelf modes

$$r^{(0)} - r_0 - \sum_m \frac{A_l k_l}{r_0 H(r_0)} \frac{\phi_m(k_l r_0)}{\omega_l} \left(m - \frac{\beta}{2\omega_l} r_0 \sin\theta_0 \right) \cos\left(m\theta_0 + \frac{\beta}{2\omega_l} r_0 \cos\theta_0 + \omega_l t_0 + \gamma_{lm} \right)$$

$$\equiv r^{(0)} - r_0' = -\sum_m \frac{A_l k_l}{r_0 H(r_0)} \frac{\phi_m(k_l r_0)}{\omega_l} \left(m - \frac{\beta}{2\omega_l} r_0 \sin\theta_0 \right) \cos\left(m\theta_0 + \frac{\beta}{2\omega_l} r_0 \cos\theta_0 + \omega_l t + \gamma_{lm} \right), \qquad \text{(C5)}$$

(Click the equation graphic to enlarge/reduce size)

$$\theta^{(0)} - \theta_0 + \sum_m \frac{A_l}{r_0 H(r_0)\omega_{lm}} \left[k_{lm}\phi_m'(k_l r_0) \sin\left(m\theta_0 + \frac{\beta}{2\omega_l} r_0 \cos\theta_0 + \omega_l t_0 + \gamma_{lm} \right) \right.$$

$$\left. + \frac{\beta}{2\omega_l} \cos\theta_0 \phi_m(k_l r_0) \cos\left(m\theta_0 + \frac{\beta}{2\omega_l} r_0 \cos\theta_0 + \omega_l t_0 + \gamma_{lm} \right) \right]$$

$$\equiv \theta^{(0)} - \theta_0' = \sum_m \frac{A_l}{r_0 H(r_0)\omega_l} \left[k_l \phi_m'(k_l r_0) \sin\left(m\theta_0 + \frac{\beta}{2\omega_l} r_0 \cos\theta_0 + \omega_l t + \gamma_{lm} \right) \right.$$

$$\left. + \frac{\beta}{2\omega_l} \cos\theta_0 \phi_m(k_l r_0) \cos\left(m\theta_0 + \frac{\beta}{2\omega_l} r_0 \cos\theta_0 + \omega_l t + \gamma_{lm} \right) \right]. \qquad \text{(C6)}$$

(Click the equation graphic to enlarge/reduce size)

Figures
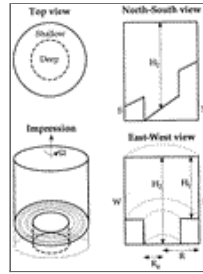
Click on thumbnail for full-sized image.

Fig. 1. Sketch of laboratory domain with abrupt shelf topography and deep interior-ocean and shallow-shelf slopes mimicking β: H_1 is the shelf depth, H_2 the ocean depth; R and R_s are the radii of domain and shelf break, respectively.
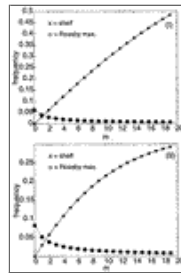
Click on thumbnail for full-sized image.

Fig. 2. Dispersion diagrams for shelf (crosses) and Rossby waves (circles) separately, frequency versus azimuthal wave number m. (Lines have been added to please the eye.) (I) Ocean analogue with shelf depth $H^*_1 = 300$ m, interior depth $H^*_2 = 3000$ m, $\beta * R * / f_0 = 0.3$, basin radius $R* = 1500$ km and shelf break radius $R^*_s = 1450$ km; and (II) laboratory analogue with $H_1 = 0.3$, $H_2 = 0.6$, $\beta * R * / f_0 = 0.4$, $R = 1$ and $R_s = 0.94$. Notice the overlap of the dispersion curves.
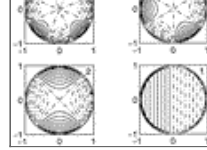
Fig. 3. Shelf modes with azimuthal mode number $m = 6, \cdots, 1$, given in a corner of each panel, for $H_1 = 0.3$, $H_2 = 0.6$, $R_s = 0.94$ and $R = 1.0$. The shelf break is indicated by a dotted line. Solid contours have positive and broken contours negative values of Ψ.
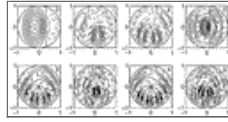
Fig. 4. Rossby modes corresponding to the eight smallest values of wavenumber k_{lm}. Corresponding m values are given in a corner of each panel.
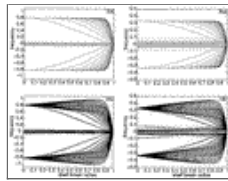
Fig. 5. (I) Ocean parameter values [see Fig. 2 (I)]. (a) Frequency dependence of pure shelf modes (dashed-dotted lines) and pure Rossby modes (horizontal dotted lines) on shelf break radius R_s separately. (b) Inviscid frequency dependence on shelf break radius of pure shelf modes (dashed-dotted lines), pure Rossby modes (straight dotted lines), and the additional hybrid Rossby–shelf modes (thick solid lines). (II) Similar for laboratory parameter values [see Fig. 2 (II)]. Shelf break radius is scaled by basin radius R. Frequency is scaled by f_0.
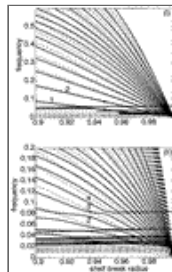
Fig. 6. Detailed sections of Fig. 5 for both (I) ocean and (II) laboratory cases. Marked by circles are selected modes subsequently analyzed at length for (I) $R_s = 0.95$ and (II) $R_s = 0.94$. Axes are again scaled by R and f_0.
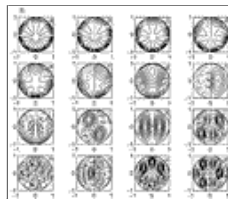
Fig. 7. Panels of 16 eigenmodes for specific shelf break radius: (I) ocean with $R_s = 0.95$ and (II) laboratory with $R_s = 0.94$. From top left to bottom right eigenfrequencies are decreasing. Notice the modified shelf nature of high-frequency eigenmodes, transitional hybrid Rossby–shelf eigenmodes, and the interior-ocean Rossby mode nature.

Fig. 7. (*Continued*)
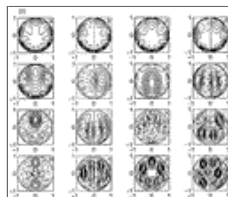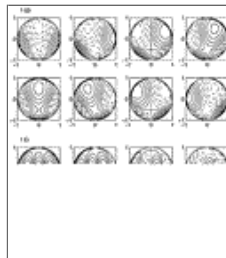
Click on thumbnail for full-sized image.

Fig. 8. Time evolution over one eigenperiod of (I) two selected ocean eigenmodes, (g), (i) in Fig. 7 ⊙ and encircled in Fig. 6 ⊙ (I), frequencies 0.0873, 0.0444; and three laboratory eigenmodes, (e)–(g) in Fig. 7 ⊙ and encircled in Fig. 6 ⊙ (II), frequencies 0.0983, 0.0831, 0.0738. Notice the hybrid nature of westward Rossby wave
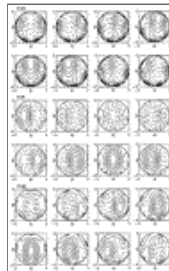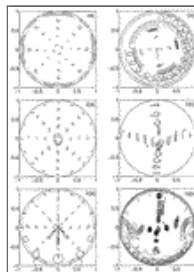

Click on thumbnail for full-sized image.

Fig. 8. (*Continued*) propagation in the northern deep interior and of shelf-break-trapped shelf mode propagation along the southern wall. In each set of eight panels time proceeds from top left to right and then bottom left to right.
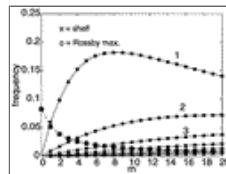
Click on thumbnail for full-sized image.

Fig. 9. Dispersion diagram for barotropic shelf (crosses) and barotropic Rossby waves (circles) in a cylinder. Frequencies are discrete and lines have been added to please the eye. Shelf wave dispersion is considered for smooth shelf topography (no β): $H(r) = H_2$ for $r < (R_s - \Delta)$, $H(r) = H_1 + (H_1 - H_2)[r - (R_s + \Delta)]/(2\Delta)$ for $(R_s - \Delta) < r < (R_s + \Delta)$, $H(r) = H_1$ for $r > (R_s + \Delta)$. Planetary Rossby waves arise due to the β effect (flat bottom). Frequency is scaled by f_0. $R* = 16.75$ cm; $R_s = 0.85$, $H_1 = 0.3$, $H_2 = 0.6$, $\Delta = 0.08$. (Numerical solution in radial direction following Staniforth et al. 1993.)

Click on thumbnail for full-sized image.

Fig. 10. (a) Harmonic fluid parcel oscillations and (b) full particle paths for (i) laboratory shelf mode $m = 4$, (ii) laboratory Rossby-mode k_{00}, and (iii) the combination of these two: the hybrid Rossby–shelf mode indicated by 4 in Fig. 6 ⊙ (II).
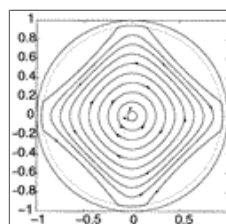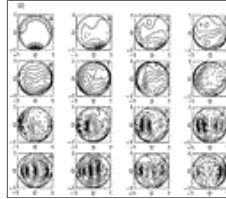

Click on thumbnail for full-sized image.

Fig. 11. Full particle path for shelf mode in Fig. 10(i)(b) ⊙ in a reference frame rotating with the angular phase speed of the mode. Time 0–480.
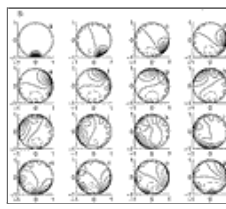
Fig. 12. Laboratory initial value problem. Panels show streamfunction starting with as initial state an anomaly at the southern shelf wall and subsequent snapshots 20 time units $1/f_0$ apart. Maximum of initial disturbance is unity. Parameter values as in Fig. 2 ⌕ (II). (i) Exact pure shelf mode solution with no β effect. (ii) Numerical finite-element hybrid Rossby–shelf mode solution.
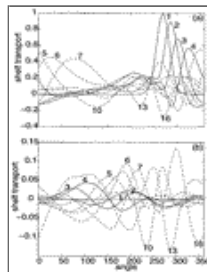
Fig. 12. (*Continued*)
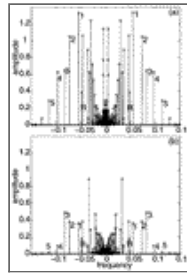
Fig. 13. Amplitudes of eigenmodes for (a) a southern anomaly and (b) an axisymmetric anomaly as initial conditions, respectively.

Fig. 14. Shelf-break-transport streamfunction at various times, starting with initial condition with 1 at $t = 0$, 2 at $t = 20$ etc., for (a) a southern shelf anomaly, and (b) an axisymmetric interior anomaly. Curves 1–4 are solid lines, curves 5–7 dashed, and curves 10, 13, and 16 are dashed-dotted lines.
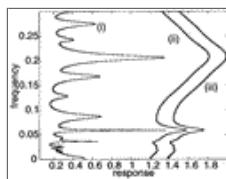
Fig. 15. Response versus forcing frequency of an ocean forced by a harmonically oscillating zonal sinusoidal windstress. Damping and windstress values are (i) $\kappa = 10^{-5}, \mu = 10^{-7}$; (ii) $\kappa = 10^{-5}, \mu = 10^{-8}$; and (iii) $\kappa = 10^{-6}, \mu = 10^{-7}$. The abscissa is response $\times 10^{-7}$. Response (ii) is multiplied by 10 and offset by 0.36 and response (iii) is multiplied by 100 and offset by 0.54. Remaining parameter values as in Fig. 2 (I) ⌕.
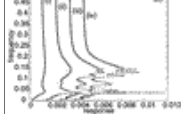
Click on thumbnail for full-sized image.

Fig. 16. Response versus forcing frequency for laboratory flow (II): (a) forced by a harmonically oscillating zonal sinusoidal wind stress at the upper lid with $\kappa = 0.0008, 0.001\ 65, 0.0033$. The abscissa is response $\times 10^{-3}$. (b) Forced topographically by $h_T = \cos(m\theta)\cos(\sigma t)$ with κ: (i) 0.000 33, (ii) 0.0001, (iii) 0.000 05, (iv) 0.000 033; and $\gamma = 0.15$. Remaining parameter values as in Fig. 2 ⊙▬ (II).
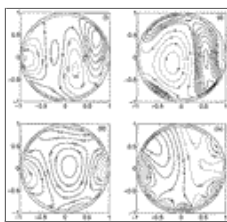
Click on thumbnail for full-sized image.

Fig. 17. Streamfunction fields corresponding to resonant peaks numbered by (i) 1 with $\kappa = 0.0033$, (ii) 2 with $\kappa = 0.001\ 65$, (iii) 3 with $\kappa = 0.0033$, and (iv) 4 with $\kappa = 0.0008$ in Fig. 16a ⊙▬. Contours scaled by: (i) 10^{-3}, (ii) 10^{-4}, (iii) 10^{-3}, and (iv) 10^{-4}, respectively.

Corresponding author address: Dr. Onno Bokhove, School of Mathematics, University Walk, Bristol BS8 1TW, United Kingdom.

E-mail: o.bokhove@bristol.ac.uk

top ▲